Atmos. Meas. Tech. Discuss., 8, 2555–2589, 2015
www.atmos-meas-tech-discuss.net/8/2555/2015/
doi:10.5194/amtd-8-2555-2015

Atmospheric Measurement Techniques Discussions
Open Access

Shortwave surface radiation budget network for observing small-scale cloud inhomogeneity fields

B. L. Madhavan[1], **J. Kalisch**[2], **and A. Macke**[1]

[1]Leibniz-Institute for Tropospheric Research (TROPOS), Permoserstraße 15, 04318 Leipzig, Germany
[2]Carl von Ossietzky University Oldenburg, Oldenburg, Germany

Received: 24 September 2014 – Accepted: 17 February 2015 – Published: 9 March 2015

Correspondence to: B. L. Madhavan (madhavan.bomidi@tropos.de)

Published by Copernicus Publications on behalf of the European Geosciences Union.

Abstract

As part of the **H**igh Definition Clouds and Precipitation for advancing Climate Prediction **O**bservational **P**rototype **E**xperiment (HOPE), a high spatial density network of 99 silicon photodiode pyranometers was set up around Jülich (10 km × 12 km area) from April to July 2013, to capture the variability in the radiation field at the surface induced by small-scale cloud inhomogeneity. Each of these autonomously operated pyranometer stations was equipped with weather sensors for simultaneous measurements of ambient air temperature and relative humidity. In this paper, we provide the details of this unique setup of the pyranometer network and the data analysis with initial quality screening procedure we adopted. We also present some exemplary cases consisting of the days with clear, broken cloudy and overcast skies to assess our spatio-temporal observations from the network, and validate their consistency with other collocated radiation measurements available during the HOPE period.

1 Introduction

Solar radiation reaching the Earth's surface is significantly modulated by direct and indirect multiple interactions with clouds, that are highly variable in space and time. These interactions and other inter-linked processes contribute to the redistribution of global radiative energy and hydrological balances in the Earth's atmosphere that govern the climate system (Stephens, 2005). One of the most critical and less understood aspects of uncertainty in climate simulations is the role of cloud-radiative processes and their interplay with precipitation (Boucher et al., 2013). Clouds scatter incoming solar radiation, reduce the shortwave irradiance reaching the Earth's surface and absorb upward longwave radiation emitted by the lower atmosphere and surface. A particularly sensitive component of incoming solar radiation that can trace the cloud inhomogeneity fields at the surface is the "*global horizontal irradiance*" (G), also referred to as "*surface insolation*". This is the total shortwave irradiance from the hemisphere above the horizontal plane surface, and includes both the direct and diffuse components of the incident radiation (WMO, 2008). Apart from radiative research interests, the spatio-temporal measurements of surface insolation are of interest to solar power plants (Robles Gil, 2007), crop yield prediction and water resource management (Roebeling et al., 2004), as well as for improving numerical weather prediction models (van den Hurk et al., 1997).

Various ground networks with sparsely distributed radiation sensors were available from the past several decades, namely, the Canadian radiation network operated by the Meteorological Service of Canada (Barker et al., 1998), WMO's Baseline Surface Radiation Network (BSRN) (Ohmura et al., 1998), and DOE's Atmospheric Radiation Measurement (ARM) Program (Michalsky et al., 1999), NOAA's SURFRAD network (Augustine et al., 2000) to quantify the Earth's radiation budget, validate satellite derived products and climate model simulations, and detect climate change signals in long-term records. However, the large uncertainties in the surface radiation budget are still less quantified than the top-of-atmosphere (TOA) budget (Wild et al., 2013). To complement these surface radiation networks, various methods were developed to derive shortwave surface irradiance using both polar-orbiting and geostationary satellite observations (e.g., Schmetz, 1989; Pinker et al., 1995). Surface solar irradiances derived from the cloud properties retrieved from METEOSAT Second Generation Spinning Enhanced Visible and Infrared Imager (MSG SEVIRI) showed that the retrievals are comparable to those measured with first-class ground based instruments by 5 % of their daily means in summer; while the accuracy is reduced significantly by a factor of 3–4 in winter owing to low solar elevation and large satellite viewing angles over the Netherlands (Deneke et al., 2008). In addition, these existing meteorological satellite imagers use 1-D radiative transfer with an assumption that clouds are plane-parallel and horizontally homogeneous to retrieve the cloud properties. Such simplified representation of spatially inhomogeneous clouds in radiative transfer models lead to systematic errors when calculating broadband

AMTD
8, 2555–2589, 2015

radiative fluxes (Scheirer and Macke, 2003). Further, the 3-D cloud radiative effects also lead to significant biases in satellite derived surface irradiances that are sensitive to viewing and solar geometry (Kato et al., 2006). In most cases, clouds with significant small-scale variability, horizontal photon transport and radiative smoothing tend to dissociate variations in TOA reflectance with transmittance from surface measurements (Barker and Li, 1997; Deneke et al., 2009). Small clouds and sub-pixel cloud variability often increase uncertainties on spatial scales at or below the resolution of satellite images (Koren et al., 2008). Thus, there is a definite need for dense surface radiation networks for resolving cloud-induced variations at the sub-scale satellite pixel resolution.

Clouds are simulated poorly in the existing global climate models (GCMs) because of their coarse spatial resolution of grid boxes. The processes important for cloud formation happen at much smaller scales, and are often difficult to represent clouds and these small-scale processes with mean grid-box properties. With a view towards improving the cloud-precipitation processes in climate model simulations, the "**H**igh **D**efinition **C**louds and **P**recipitation for advancing **C**limate **P**rediction" (HD(CP)^2) project (http://hdcp2.eu/) was funded by the Federal Ministry of Education and Research (BMBF), Germany. This initiative includes various modules focused on: Modelling (M), Observations (O) and Synthesis (S). In order to access the 3-D structure of clouds at HD(CP)^2 model resolution, the **H**D(CP)^2 **O**bservational **P**rototype **E**xperiment (HOPE) was designed as part of the observation module to measure the sub-grid scale variability of dynamical, thermodynamical and cloud micro-physical properties with 1 m spatial and 1 s temporal resolution. This HOPE measurement campaign was conducted around the super-site JOYCE (Jülich ObservatorY for Cloud Evolution) with an aim to provide data sets for critical model evaluation at the scales of model simulation. Further information on the sub-grid scale variability and micro-physical properties that are subject to parametrizations at high resolution will be explored. Within the observational sub-module (O4), entire measurements were classified into five work packages focused on land-surface exchange processes (WP1), planetary boundary layer studies (WP2), aerosol and cloud micro-physics (WP3), cloud morphology (WP4) and radiative closure studies (WP5). Leading into WP5, our focus was to probe the spatio-temporal variability of cloud induced radiation fields at the surface with a resolution comparable to or even better than $HD(CP)^2$ model. See Macke and HOPE-Team (2015) for an overview on the HOPE campaign and preliminary results.

In this context, the present paper is aimed at providing an overview on our experimental contribution towards setting up of the surface radiation network with finer scales of spatial and temporal resolution during HOPE. The outline of this paper is as follows: in Sect. 2, details about instrumentation and experimental setup are described. Data analysis and initial quality screening procedure details are given in Sect. 3. In Sect. 4, we mainly focus on exploring some of the days with clear sky, broken cloudy and overcast conditions to evaluate our spatio-temporal measurements using other collocated radiation measurements from the supersites. Finally, conclusions and a brief outlook are presented in Sect. 5.

2 Instrumentation, experimental setup and data availability

2.1 Pyranometer Network (PyranoNET)

To observe the small-scale variability of cloud induced shortwave surface radiative forcing at high spatio-temporal resolution, we developed a set of 100 autonomous pyranometer stations equipped with meteorological sensors (relative humidity and air temperature) for HOPE campaign. Each station is built with the following main components:

i. An EKO silicon photodiode pyranometer (Model: ML-020VM) for measuring the shortwave global irradiance (G in $\mathrm{W\,m^{-2}}$) in the spectral range 0.3–1.1 µm. The limited spectral range is a well-known limitation of this type of pyranometer caused due to the spectral response of the photodiode. More details on the calibration and spectral responsivity of the ML-020VM silicon photodiode sensors is given

AMTD
8, 2555–2589, 2015

in Appendix A. In comparison to the thermopile pyranometers, silicon photodiode sensors have a superior response time enabling to a sampling frequency of 10 Hz, which allows it to follow the rapid changes in the sky. Further specification details are listed in Table 1.

ii. A micro-module (Model: Driesen+Kern DKRF 4001-P) combines air temperature and relative humidity (RH) sensors for meteorological measurements. While the temperature sensor has a measurement range from 253.15 to 353.15 K (i.e., –20 to +80 °C), RH sensor measurements range from 0 to 100 %. The accuracy of temperature measurement is ± 1.5 K at 233.15 K, decreases linearly to ± 0.5 K at 273.15 K and remain stable up to 313.15 K, and again increases linearly to ± 1.5 K at 353.15 K. The accuracy of the RH measurement is ± 3.5 % at 0 % RH, decreasing linearly to ± 2 % at 10 % RH to remain stable until 90 %, and thereafter increases linearly reaching ± 3.5 % at 100 % RH.

iii. A compact GPS receiver module (Model: Fastrax UP501) with embedded GPS antenna for reliable timing and positioning information. The output data is in accordance with NMEA 0183 protocol.

iv. A micro-controller ARM7-based data logger board (Model: Sparkfun Electronics Logomatic v2) with a built-in micro-SD socket is used to save data onto an SD card.

v. A power supply unit (i.e., 6 V/19 Ah Zinc carbon VARTA 4R25-2 battery) with a lifetime of 10 days enables continuous usage.

A pyranometer station in the field during observation and the schematic of data flow from pyranometer through logger to memory storage device is shown in Fig. 1. The data logger software has been modified to enable simultaneous logging of the serial (GPS module) and analog (pyranometer, temperature and RH modules) data. The logger's internal real-time clock is synchronized with the GPS time frequently and all the data is stored on a micro-SD card (∼ 2 GB). The voltage signal detected by

AMTD
8, 2555–2589, 2015

Title Page
Abstract | Introduction
Conclusions | References
Tables | Figures
◀| |▶
◀ ▶
Back | Close
Full Screen / Esc
Printer-friendly Version
Interactive Discussion

each pyranometer sensor ranges from 0 to 10 mV (∼ 0 to 1400 W m^{-2}) and an amplifier (INA333) enhances the signal by a factor of 300 to convert the signal in the range of 0–3 V. Note that the amplification of the pyranometer signal is independent of fading battery voltage because the stabilized output voltage (3.3 V) of the data logger board is used. If the battery voltage is too weak, then the whole logger board does not work anymore. In case of temperature and RH sensors, their respective measurement ranges are related with the output voltage from 0 to 2.5 V. These voltage signals are scaled to 10 bit counts ranging from 0 to 1023 and stored on the memory card.

2.2 HOPE campaign and data availability

During the HOPE campaign, we have setup 99 pyranometer stations covering the spatial domain 50.85–50.95° N and 6.36–6.50° E (∼ 10 km × 12 km area) around Jülich (mostly in open farm fields). Each measurement system was placed on a mounting rod, that is approximately 1.8 m high above the ground, and provides the measurements (in 10 bit counts) corresponding to the downward shortwave global irradiance, air temperature and relative humidity at 10 Hz frequency while the GPS information (latitude, longitude, time etc.) is obtained at 1 s resolution. The spatial setup of pyranometer stations during HOPE campaign is shown in Fig. 2. The network was continuously operational from 2 April to 24 July 2013 to capture the small-scale variability of cloud inhomogeneity fields from the spatial domain that includes all stations. During the campaign, batteries were replaced every week and a record of the physical information such as cleanliness of the pyranometer glass dome (on a scale of 0–10) and level imbalance of the mounting platform (on a scale of 0–3) were noted for each station. This information was then used to assign an observational flag (“oflag” on a scale of 1–4) to the entire previous week’s data of that corresponding station. Table 2 outlines the criteria adopted for assigning these observational flags.

Sites of the Research Center Jülich (FZJ) and the Karlsruhe Institute of Technology Hambach (KIT1, KIT2) were equipped with thermopile pyranometers, whereas the site of the Leipzig Aerosol and Cloud Research Observations System (LACROS) was operating a sky imager. These collocated sites with supplementary measurements were also shown in Fig. 2. Nearest pyranometers from the network are spatially apart by 29.5, 227.5 and 343.5 m with respect to FZJ, KIT1 and KIT2 thermopile pyranometers.

3 Data processing and initial quality screening

The raw data stored in the form of 10 bit counts is converted to global-horizontal irradiance (G in W m^{-2}), ambient air temperature (T_a in K) and relative humidity (RH in %) using the following equations:

$$G = \left[\left(N_{\text{counts}} \cdot \frac{3.3}{1023}\right) \cdot \left(\frac{1}{300}\right)\right] \cdot \frac{1}{K_c} \quad (1)$$

$$T_a = \left[\left(N_{\text{counts}} \cdot \frac{3.3}{1023}\right) \cdot \left(\frac{100}{2.5}\right) - 20\right] + 273.15 \quad (2)$$

$$\text{RH} = \left[\left(N_{\text{counts}} \cdot \frac{3.3}{1023}\right) \cdot \left(\frac{1}{2.5}\right)\right] \cdot 100 \quad (3)$$

Here N_{counts} correspond to the respective measurements in 10 bit counts and K_c denote the sensitivity or calibration coefficient (in V W^{-1} m^{2}) of a pyranometer sensor. As there is no sub-second information from the GPS, both the pyranometer and meteorological measurements at 10 Hz frequency are averaged around the GPS time at 1 s resolution. In addition, the GPS provided information e.g., latitude, longitude, day and time, was used to compute the solar zenith and azimuth angles as described in Liou (2002).

At higher solar zenith angles (θ_0) and under varying sky conditions, atmospheric refraction leads to an increasing effect on the global irradiance. Since atmospheric transmittance (T) is more representative of the atmospheric column, it is derived from the global irradiance measurements by normalizing with a fixed value

Discussion Paper | Discussion Paper | Discussion Paper | Discussion Paper |
AMTD
8, 2555–2589, 2015
Shortwave surface radiation budget network
B. L. Madhavan et al.
Title Page
Abstract Introduction
Conclusions References
Tables Figures
◀| |▶
◀ ▶
Back Close
Full Screen / Esc
Printer-friendly Version
Interactive Discussion

of extraterrestrial irradiance corrected for geometrical factors. The equation for atmospheric transmittance is given below:

$$T = \frac{G'}{\left[S'_0 \cdot \left(\frac{r}{r_0}\right)^2\right] \cdot \cos\theta_0} \tag{4}$$

Here S'_0 (= 619.91 W m^{-2}) is the sensor specific extraterrestrial irradiance (i.e., at zero air mass), G' $\left(= \left(\frac{619.91}{1362.0}\right) \cdot G\right)$ is the scaled global-horizontal irradiance in the spectral sensitivity range of the sensor, r is the actual Sun–Earth distance (in astronomical units or AU), and r_0 (= 1.0 AU) is the mean Sun–Earth distance. The value of 1362.0 W m^{-2} is the climate significant total solar irradiance at the TOA (Kopp and Lean, 2011). The sensor specific extraterrestrial irradiance (S'_0) is derived from the Gueymard (2004) solar spectrum weighted by the spectral response function of the silicon photodiode sensor (see Fig. 3). If there is no atmosphere, then the transmittance will be 1 and the global irradiance equals to the direct-normal irradiance from the sun (i.e., no diffuse component). The transmittance can be less than 0.1 under very heavy overcast sky and the downward radiance distribution is almost independent of the direction.

Measurements of global-horizontal irradiance from each pyranometer station may be influenced by various *observable* and *non-observable* factors. While the *observable* factors include the level imbalance of the mounting platform, cleanliness of the pyranometer glass dome and calibration uncertainty; the *non-observable* factors can be an instrument malfunction, short-time resting of birds or insects, water drops on the glass dome (during rain, fog or dew) and background shadowing. The *observable* factors can be nullified through our observational flags (see Table 2), but the possibility of misrepresenting some of the *good* data obtained during the week as *bad* or *spurious* cannot be ignored. Over the entire HOPE period, it was observed that more than 80 stations (∼ 80 %) always had *good* data on any day.

From among the non-observable factors, the main concern was to identify malfunctioning sensors (e.g., pyranometer or RH or temperature). So, we adopt

AMTD
8, 2555–2589, 2015

a statistical screening procedure to classify each measurement as either *good*, *suspected outlier* or *outlier* (i.e., statistical flag or sflag = 1, 2, 3 respectively). To avoid any background shadowing due to closely located trees or buildings, this method was restricted on the data obtained for $\theta_0 < 75^\circ$. However, this limitation cannot guarantee that background shadowing will be eliminated completely as each station may be under the influence of a different topography. Steps involved in our statistical procedure are listed below:

i. At each time step, we determine various statistical parameters, namely, mean, median, first quartile (Q25), third quartile (Q75), minimum, maximum and inter-quartile range (IQR = Q75 − Q25) by considering measurements from all available pyranometer stations.

ii. Measurements are classified as *good*, if each individual value lies in the range: [Q25 − 1.5 · IQR, Q75 + 1.5 · IQR].

iii. Measurements are classified as *suspected outliers*, if each individual value lies in any of these ranges: [Q25 − 3·IQR, Q25 − 1.5·IQR] or [Q75 + 1.5·IQR, Q75 + 3·IQR].

iv. Measurements are classified as *outliers*, if each individual value is either above (3 · IQR + Q75) or below (3 · IQR − Q25).

All *outliers* need not be spurious measurements. Also, the possibility of small-scale cloud induced fields from a few stations being classified as *outliers* is high. So, the pyranometer stations with more than 50 % measurements classified as *outliers* or *minima* or *maxima* on a given day were ignored completely considering the chance of sensor malfunctioning. Over the entire HOPE period, we noticed that there were at most two malfunctioning stations on a day.

The following technical terminology will be used hereafter for elucidating the measurements from the pyranometer network:

a. *Range of spatial variability* denotes the difference between the maximum and minimum values at an instance of time corresponding to the spatial field of

AMTD
8, 2555–2589, 2015
Shortwave surface radiation budget network
B. L. Madhavan et al.

atmospheric transmittance (ΔT) or relative humidity (ΔRH) or air temperature (ΔT_a).

b. *Limits of spatial variability* defines the [minimum, maximum] values at an instance of time corresponding to the spatial field of the measured or derived variable.

c. *Root mean square deviation* (RMSD) represents the magnitude of variability in the time-series between the minimum and maximum values corresponding to the spatial field of the measured or derived variable.

An illustration for the above method is shown for 31 May 2013 in Fig. 4. During this day, there was some light to medium rain in the morning with rapid clearance at late afternoon (~ 16:00 UTC) followed by low-cumulus humilis clouds. In the evening, cloudiness again increased with cumulus/stratus until overcast conditions appeared. Temporal variability in the mean, median, minimum and maximum values of spatial global irradiance and derived atmospheric transmittance are shown in the Fig. 4a and b respectively. Similarly, the Fig. 4c–e shows the respective temporal variability of the spatial transmittance values by excluding the data classified as bad/missing (oflag $\neq$ 3 or 4), outliers (sflag $\neq$ 3) and malfunctioning stations. In Fig. 4f, we show the temporal range of spatial variability in atmospheric transmittance represented in Fig. 4c–e normalized with respect to that in Fig. 4b. The RMSD values of atmospheric transmittance represented in Fig. 4b–e were obtained as 0.4124, 0.4124, 0.3678 and 0.4123 respectively. This implies that the range of spatial variability represented in Fig. 4b, c and e remains the same, while there was a 10 % decrease in the corresponding RMSD value obtained from Fig. 4d. In case of observational bad or missing data (oflag = 3 or 4) and malfunctioning stations, they are station specific and thus exclude the data from identified spurious stations. In contrast, the statistical outliers (sflag = 3) are not station specific with a high probability of denoting small-scale cloud induced fields as outliers and thus reducing the data set, which was evident from the decrease in the normalized range of spatial variability (Fig. 4f). Since the physical checking of the data quality for each station requires enormous time, our current study

AMTD
8, 2555–2589, 2015

is limited to identifying and excluding the malfunctioning stations, if any, from the data sets using the statistical procedure described above.

An intra-comparison experiment among our pyranometer stations was conducted on 27 March 2013 before deploying to HOPE campaign. The RMSD between the temporal maximum and minimum values of atmospheric transmittance, relative humidity (%) and air temperature (in K) were obtained as 0.044, 6.1 % and 1.26 K respectively. Also, an inter-comparison of 1 min averages of downward shortwave irradiance measurements between our closely placed pyranometer station (i.e., PYR76) and FZJ thermopile pyranometer (Model: Kipp and Zonen CMP21), showed a very high linear correlation of 0.99 and a negative bias of 2.98 $\mathrm{W\,m^{-2}}$ (RMSD = 17.77 $\mathrm{W\,m^{-2}}$) for the entire campaign period. This is fairly within the uncertainty given by the manufacturer (see Table 2). In our case, we can expect a maximum of 10 % measurement errors from an individual pyranometer station but these are not further considered in this paper as our focus was to study the small-scale spatial and temporal variability of cloud inhomogeneity fields using the pyranometer network.

4 Results and discussion

During the HOPE campaign, a total of 18 intensive observation periods (IOPs) with variable cloudy skies were identified between April and May 2013. Over the entire observation period, there were around 10 almost clear sky days, with an exception of a few cirrus clouds in between for shorter durations on some days. The mean of daily temperatures during April–May period was observed to be 283.65 K with a minimum of 270.95 K and a maximum of 297.95 K. In addition, most of the overcast days were accompanied by precipitation. The total precipitation for April–May period was measured to be 114.7 mm. In the following sub-sections, we assess the spatio-temporal measurements of global-horizontal irradiance through derived atmospheric transmittance on different days with homogeneous and inhomogeneous sky conditions. First, we ascertain the representative time-series of spatial variability in atmospheric

AMTD
8, 2555–2589, 2015

transmittance (ΔT from the network) with the collocated measurements from thermopile pyranometers (e.g., FZJ, KIT1, KIT2). In addition, we compare the time-series measurements of the nearest pyranometers (from network) with the thermopile pyranometers (see Table 3). Finally, the instantaneous spatial inhomogeneity in atmospheric transmittance fields are compared with the corresponding sky-images (movies are included in Supplement).

4.1 Clear sky – 4 May 2013

It is very essential to understand the consistency in clear-sky atmospheric transmittance among a large number of measurement stations as it offers a possibility for validating the existing clear sky models. These models are required to study the more complicated cloudy skies in terms of the cloud radiative forcing. In a study focused on comparing the downward shortwave irradiance measurements on clear sky days with six different models during an aerosol intensive observation period at Southern Great Plains in 2003, biases with a maximum of 1 % for direct and less than 1.9 % for diffuse were observed (Michalsky et al., 2006). Neglecting these uncertainties may sometimes lead to substantial errors in clear sky radiative transfer parametrizations. By using the measurements on multiple clear sky days, one can obtain the differences between the modeled and observed clear sky global-horizontal irradiance at each station and thus estimate the overall variability in the flux measurements to expose background shadowing.

In Fig. 5a, we show the instantaneous spatial variability in the derived atmospheric transmittance on a clear sky day (4 May 2013) along with the corresponding sky image (Fig. 5b) obtained at the LACROS site. During this day, only few high cirrus clouds were seen in the morning and thereafter perfect clear sky conditions prevailed with weak westerly winds. Both RH and temperature measurements showed consistency in the range of spatial variability from 10 to 20 % and 6 to 8 K respectively during the day. At noon (~ 14:00 UTC), RH varied from 35 to 55 % while temperature ranged from 289 to 295 K in the observation domain.

AMTD
8, 2555–2589, 2015
Shortwave surface radiation budget network
B. L. Madhavan et al.

The temporal variability in the mean, median, minimum and maximum values of the derived atmospheric transmittance from the spatial domain is shown in Fig. 5c. In the observation domain, ΔT varied between 0.11 and 0.77 (RMSD = 0.39). Apart from the contribution due to aerosols on clear sky day, it is possible that the large spread in the morning and evening times can be due to the larger directional errors of pyranometers for lower solar elevation angles. In our case, we have observed that a few stations were influenced by the background shadowing from surrounding obstructions (see "movie01.avi" in Supplement). Also, the short-time decrements in transmittance from some stations may be due to the resting of birds randomly. On any homogeneous day, these spurious fluctuations in the retrieved transmittance values were automatically classified as *outliers* through our statistical procedure. By ignoring these *outliers*, we observed a decrease in ΔT to vary between 0.025 and 0.38. The temporal variability in the mean and median of spatial atmospheric transmittance values concurred well with a high degree of linear correlation (= 0.99) and negligible variance (= 0.005) implicating that these spatial measurements are evenly distributed around the mean.

The time-series comparison of derived atmospheric transmittance values from collocated thermopile pyranometers (i.e., FZJ, KIT1, KIT2) with our close-by stations showed a very good match-up (see Table 3). However, an approximate 5 % difference was observed consistently between the spatial mean transmittance based on the network and the thermopile pyranometer measurements especially during 09:00–15:00 UTC. The frequency distribution of instantaneous spatial atmospheric transmittance values shown in Fig. 5d indicated a dominant mode centered around 0.7. During this day, the peak of the dominating mode varied around 0.4–0.7 transmittance.

4.2 Broken cloudy sky – 5 May 2013

Under broken cloud conditions, the pyranometer views a portion of clear sky or even direct sunlight. Further, the diffuse irradiance decreases rapidly as patches of clear sky enter the field of view of the pyranometer. This is because the diffuse irradiance from a clear sky is smaller than that of a cloudy sky, if the clouds are not too thick. Broken

AMTD
8, 2555–2589, 2015

clouds vary considerably in their horizontal and vertical extents. For inhomogeneous clouds, determination of the flux absorbed in a cloud layer is complicated by the horizontal leakage of photons. In addition, the uncertainties in the input parameters required for radiative transfer calculations result in errors that are comparable or even larger than the discrepancies between observed and computed cloud absorptions. So, the cloud inhomogeneity has a significant influence on broadband solar fluxes (Long and Ackerman, 2000; Scheirer and Macke, 2003).

The instantaneous spatial variability in the derived atmospheric transmittance on a broken cloudy day (5 May 2013) is shown in Fig. 6a along with the corresponding sky image in Fig. 6b. On this day, clear sky conditions prevailed till 09:00 UTC and thereafter slightly increasing cloudiness with cumulus humilis was observed. The winds turned from south in the morning to west during noon and then to north. Both RH and temperature measurements indicate consistency in the range of spatial variability. At noon ($\sim$ 14:00 UTC), the RH and temperature measurements varied from 35 to 60 % and 291 to 297 K respectively in the observation domain.

The temporal variability in the mean, median, minimum and maximum values of the derived atmospheric transmittance from the spatial domain is shown in Fig. 6c. During this day, ΔT varied between 0.16 and 0.89 with an RMSD of 0.63 (see "movie02.avi" in Supplement). The large spatial heterogeneity in atmospheric transmittance values is more pronounced through the incoherent variability between different thermopile pyranometers (at FZJ, KIT1, and KIT2). Occassional decoupling between the mean and median time-series occurred when the sky was covered with broken clouds. However, a high correlation (= 0.904) with negligible variance (= 0.047) prevailed between them (see Table 3). If the median is higher than mean, then most of the spatial atmospheric transmittance values are higher than the mean value and this implies that the cloud cover in the sky is lower than the clear sky portion.

The time-series comparison of derived atmospheric transmittance values from collocated thermopile pyranometers with our close-by stations indicated large deviations during the periods of broken cloud cover (Table 3). However, the transmittance from thermopile pyranometers always lie within the limits of spatial variability from pyranometer network. This indicates that our pyranometer network is well capturing the cloud inhomogeneity fields at the surface. The frequency distribution of instantaneous spatial atmospheric transmittance values (Fig. 6d) indicated a bi-modal distribution with a significant mode at higher transmittance value (∼ 0.7) and an insignificant mode at lower transmittance value (∼ 0.2). The dominance of a mode at higher transmittance values indicates more hemispheric clear sky with lesser cloud cover.

4.3 Overcast sky – 30 May 2013

An overcast sky is characterized by relatively high irradiance (spectral) towards the shortwave end of the spectrum compared to the corresponding spectrum for a clear sky. For horizontally homogeneous and non-precipitating clouds with high liquid water content, solar flux absorbed by clouds will be equal to the difference between simultaneous and collocated measurements of net radiative fluxes observed at the upper and lower bounds of a cloud layer. Most often these differences are noisier than the original flux measurements, owing to the loss in significant digits. With thick overcast conditions, atmospheric transmission can reduce to less than 10 % of it's clear sky value.

The instantaneous spatial variability in the derived atmospheric transmittance on an almost overcast day (30 May 2013) is shown in Fig. 7a along with the representative sky image (Fig. 7b). During this day, strong cloudiness prevailed mostly with few clearings in between. Winds from south were prevailing throughout the day. As there was rain in the previous night and early morning, significant range of spatial variability in RH was observed (between 20 and 40 %). While RH values varied between 40 and 80 % during the day, temperature remained consistent and homogeneous with 6 K as the maximum range of spatial variability.

The temporal variability in the mean, median, minimum and maximum values of the derived atmospheric transmittance from the spatial domain is shown in Fig. 7c.

AMTD
8, 2555–2589, 2015

During this day, ΔT varied from 0.12 to 1.13 with an RMSD of 0.53 (see "movie03.avi" in Supplement). The time-series of spatial mean and median transmittance values concurred well with a very high correlation (= 0.96) and a minimal variance (= 0.012) indicating an uniform distribution of cloudy transmittance values around the mean. Throughout the day, dominance of lower atmospheric transmittance values (< 0.5) in the spatial domain indicate the homogeneity in overcast cloud cover in the sky. Very high atmospheric transmittance values (> 1.0) were observed in the morning before 08:30 UTC during the periods of short clearances in the sky (i.e., broken clouds). At this time, the global-horizontal irradiance observed at the surface was higher for some stations than the corresponding TOA values. It is possible that for short time-periods under broken cloudy conditions, the downward global irradiance at the surface can be larger than that at the top-of-atmosphere (TOA) due to the multiple reflections from the cloud edges (i.e., broken cloud effect) that are not in the way of incident solar beam (Shi et al., 2008). This was also pronounced with the collocated thermopile pyranometers (KIT1 and KIT2).

The time-series comparison of derived atmospheric transmittance from thermopile pyranometers with nearby network stations indicated high correlation > 0.82 (Table 3). In addition, measurements from thermopile pyranometers showed a consistency throughout the time period lying within the limits of spatial variability. The frequency distribution of instantaneous spatial atmospheric transmittance values from the network (Fig. 7d) indicated a mono-modal distribution with significant peak at lower transmittance values (~ 0.3) during overcast conditions. However, during shorter clearances (before 08:30 UTC) with broken clouds a bi-modal distribution was observed with dominant mode at lower transmittance values.

5 Conclusions and outlook

The spatial and temporal distribution of shortwave surface global irradiance measurements obtained during the HOPE campaign with unprecedented resolution

AMTD
8, 2555–2589, 2015

provides a unique observational data set aimed at capturing the small-scale modulations of radiation due to clouds and their inhomogeneity. This paper motivates the need for a small-scale high density radiation network and presents some of the first results of the spatio-temporal variations in the derived atmospheric transmittance values based on our pyranometer network. The performance of initial quality screening procedure depends on various factors influencing the measurements. As a future work, we will look into the absolute accuracy of these silicon photodiode measurements more closely with data from another field campaign (e.g., HOPE-Melpitz) that includes measurements from a collocated BSRN-like radiation station. Summarizing, the preliminary observations are outlined in the following:

i. Significant spatial and temporal variability in the retrieved atmospheric transmittance fields was observed during broken cloudy conditions.

ii. The collocated thermopile pyranometers provided reference data and showed a good agreement by lying within the limits of spatial variability in the derived atmospheric transmittance from the network under different sky regimes.

iii. For a homogeneous sky condition (clear or overcast), a distinct mono-modal spatial distribution of atmospheric transmittance was observed.

iv. For an inhomogeneous sky condition (broken clouds), a bi-modal spatial distribution of atmospheric transmittance was observed with dominant mode characterized by the relative contribution due to clear and cloudy portions of sky.

Extensive spatio-temporal analysis between the cloud induced transmittance fields derived from the measurements of our pyranometer network and the corresponding TOA reflectance from the high-resolution broadband channel (0.4–1.1 µm) of METEOSAT SEVIRI can possibly ensure the quality of our measurements. Most importantly, by performing multi-scale analysis (Deneke et al., 2009) of these measurements from HOPE campaign, the optimal spatial and temporal resolutions required for probing the small-scale cloud radiative effects under different cloud regimes in the sky can be understood. A recent study by Hinkelman (2013) found that the correlation between the irradiances at two different sites depends on the orientation of the axis between them relative to the wind direction and on their spatial separation.

During the HOPE campaign, state-of-the-art remote sensing instrumentation were used to observe a large atmospheric volume with high frequency. This experiment will allow for model evaluation at the scale of HD(CP)^2 model simulations and even provide information on the sub-grid scale variability and the micro-physical properties that will remain subject to parametrizations. In this context, a radiative closure study is an essential tool to evaluate the accuracy of atmospheric retrievals (e.g., cloud and aerosol properties) and measurement techniques. Radiative transfer models can also be validated through focused closure studies using well defined cases and high quality measurements. While the clear sky radiation field over a homogeneous surface is well understood and can be simulated with one dimensional radiative transfer, the situation becomes complicated and more challenging for cloud fields which requires three dimensional (3-D) radiation transfer. The quality controlled measurements from our pyranometer network will be used to perform radiative closure studies using 3-D Monte Carlo radiation transfer code (Macke et al., 1999). For this, the cloud fields from existing LES simulations at different spatial scales will be used as input in the Monte Carlo radiation transfer to understand the uncertainty in cloud radiative forcing and thus improve the radiation parametrizations at sub-scales for better climate predictions.

Appendix A: Calibration and spectral responsivity of the ML-020VM silicon photodiode pyranometer

The EKO ML-020VM silicon photodiode pyranometers were calibrated against a *reference* ML-020VM sensor under an indoor solar simulator. The *reference* sensor was calibrated against a *reference* thermopile pyranometer. In our case, the calibration factor (or sensor sensitivity) is a single number determined under standard conditions

AMTD
8, 2555–2589, 2015

with a specific spectrum that converts the narrowband response to an equivalent broadband response. The ML-020VM pyranometer sensors used during HOPE campaign have calibration factors in the range between 6.3 and 7.7 $\mu V W^{-1} m^2$ (provided by the manufacturer). Though the effect of aerosols in the visible solar spectrum under broken cloud conditions is within the sensor spectral sensitivity, the influence of optical thickness, thermodynamic phase and effective radius of the cloud particles in near-infrared solar spectrum are not accounted for in the measurement range of silicon photodiode sensor. So, we convolute the standard solar spectrum of Gueymard (2004) (scaled such that the integral is 1362.0 $W m^{-2}$) with the EKO silicon photodiode spectral response function (see Fig. 3) and then integrate the weighted EKO solar spectrum over the range of sensitivity to calculate the sensor specific extraterrestrial irradiance (S'_0) using the following equation:

$$S'_0 = \int_{\lambda_1}^{\lambda_2} \Phi(\lambda)\eta(\lambda)\mathrm{d}\lambda \tag{A1}$$

Here λ_1 and λ_2 are the lower and upper spectral limits (in µm), Φ is the extraterrestrial solar spectrum (in $W m^{-2} \mu m^{-1}$) at a Sun–Earth distance of 1 AU, and η denotes the spectral response function of EKO silicon photodiode sensor. This sensor specific extraterrestrial irradiance (S'_0) is used while deriving atmospheric transmittance (T) in Eq. (4).

Some studies indicated that the spectral dependency of Silicon photodiode sensors on daily solar zenith angle remains to play a significant role (Myers, 2011; Sengupta et al., 2012). But there is no method to correct for it unless the solar spectrum for each measurement condition is known exactly. Alternately, the compensation for the influence of the time-of-day dependent solar spectrum can be possible by using an empirically determined function (King et al., 1998). For EKO silicon photodiode sensors, the spectral error will be in the order of 2–5 % during the day (see Table 1). Accuracy of these global irradiance measurements from silicon photodiode sensors

AMTD
8, 2555–2589, 2015

depend on the systematic influences associated with solar spectrum, solar angle of incidence and temperature (King and Myers, 1997). As the stability is expected to change by about 1 % over a year, it is not reasonable to make a linear prediction and thus these sensors need to be re-calibrated once per two years. Also, the well-known uncertainties of silicon photodiode sensors, namely, temperature-dependence of sensor response, cosine response errors, varying spectral atmospheric conditions etc. reported in various studies (Dirmhirn, 1968; Michalsky et al., 1987, 1991; King and Myers, 1997) are not accounted for in this study.

The Supplement related to this article is available online at doi:10.5194/amtd-8-2555-2015-supplement.

Acknowledgements. The authors acknowledge essential technical support from the TROPOS mechanics and electronics workshops in designing and building the autonomous pyranometer. Many thanks to all the private land owners for their support. We are grateful to Research Center Jülich (FZJ) for valuable logistic support in setting up and maintaining the instruments. The first author's work was funded by Federal Ministry of Education and Research (BMBF), Germany as part of HD(CP)^2 project. We also thank our colleagues Hartwig Deneke, Sebastian Bley, Felix Dietzsch, Daniel Merk, Jonas Walther, Alexander Graf (FZJ), Michael Eickmeier and Felix Peintner for extending their support during HOPE campaign. We thank Birger Bohn from FZJ, and Vera Maurer and Norbert Kalthoff from KIT for sharing their pyranometer data sets. We appreciate the support provided by Alexander Los and Kees Hogendijk from EKO Instruments, the Netherlands.

References

Augustine, J. A., DeLuisi, J. J., and Long, C. N.: SURFRAD – a national surface radiation budget network for atmospheric research, B. Am. Meteorol. Soc., 81, 2341–2357, doi:10.1175/1520-0477(2000)081<2341:SANSRB>2.3.CO;2, 2000. 2557

Barker, H. W. and Li, Z.: Interpreting shortwave albedo-transmittance plots: true or apparent anomalous absorption?, Geophys. Res. Lett., 24, 2023–2027, doi:10.1029/97GL02019, 1997. 2558

Barker, H. W., Curtis, T. J., Leontieva, E., and Stamnes, K.: Optical depth of overcast cloud across Canada: estimates based on surface pyranometer and satellite measurements, J. Climate, 11, 2980–2994, doi:10.1175/1520-0442(1998)011<2980:ODOOCA>2.0.CO;2, 1998. 2557

Boucher, O., Randall, D., Artaxo, P., Bretherton, C., Feingold, G., Forster, P., Kerminen, V. M., Kondo, Y., Liao, H., Lohmann, U., Rasch, P., Satheesh, S. K., Sherwood, S., Stevens, B., and Zhang, X. Y.: Clouds and aerosol, in: Climate Change 2013: The Physical Science Basis. Contributions of Working Group I to the Fifth Assessment Report of the Intergovernmental Panel on Climate Change, edited by: Stocker, T. F., Qin, D., Plattner, G.-K., Tignor, M., Allen, S. K., Boschung, J., Nauels, A., Xia, Y., Bex, V., and Midgley, P. M., Tech. rep., IPCC, Cambridge University Press, Cambridge, UK, New York, NY, USA, 571–657, 2013. 2556

Deneke, H. M., Feijt, A. J., and Roebeling, R. A.: Estimating surface solar irradiance from METEOSAT SEVIRI-derived cloud properties, Remote Sens. Environ., 112, 3131–3141, doi:10.1016/j.rse.2008.03.012, 2008. 2557

Deneke, H. M., Knap, W. H., and Simmer, C.: Multiresolution analysis of the temporal variance and correlation of transmittance and reflectance of an atmospheric column, J. Geophys. Res., 114, D17206, doi:10.1029/2008JD011680, 2009. 2558, 2572

Dirmhirn, I.: On the use of silicon cells in meteorological radiation studies, J. Appl. Meteorol., 7, 702–707, 1968. 2575

Gueymard, C.: The Sun's total and spectral irradiance for solar energy applications and solar radiation models, Sol. Energy, 76, 423–452, 2004. 2563, 2574, 2585

Hinkelman, L. M.: Differences between along-wind and cross-wind solar irradiance variability on small spatial scales, Sol. Energy, 88, 192–203, doi:10.1016/j.solener.2012.11.011, 2013. 2573

Kato, S., Hinkelman, L., and Cheng, A.: Estimate the satellite derived cloud optical thickness and effective radius errors and their effect on computed domain averaged irradiances, J. Geophys. Res., 111, 17201–17217, doi:10.1029/2005JD006668, 2006. 2558

King, D. L. and Myers, D. R.: Silicon-photodiode pyranometers: operational characteristics, historical experiences, and new calibration procedures, in: Twenty-Sixth IEEE Photovoltaic Specialists Conference, Anaheim, CA, 29 September–3 October, 1285–1288, doi:10.1109/PVSC.1997.654323, 1997. 2575

AMTD

8, 2555–2589, 2015

Title Page
Abstract | Introduction
Conclusions | References
Tables | Figures
◀| |▶
◀ ▶
Back | Close
Full Screen / Esc
Printer-friendly Version
Interactive Discussion

King, D. L., Boyson, W. E., Hansen, B. R., and Bower, W. I.: Improved accuracy for low-cost solar irradiance sensors, in: 2nd World Conference and Exhibition on Photovoltaic Solar Energy Conversion, Vienna, Austria, 6–10 July, 1947–1952, 1998. 2574

Kopp, G. and Lean, J. L.: A new, lower value of total solar irradiance: evidence and climate significance, Geophys. Res. Lett., 38, L01706, doi:10.1029/2010GL045777, 2011. 2563

Koren, I., Oreopoulos, L., Feingold, G., Remer, L. A., and Altaratz, O.: How small is a small cloud?, Atmos. Chem. Phys., 8, 3855–3864, doi:10.5194/acp-8-3855-2008, 2008. 2558

Liou, K. N.: An Introduction to Atmospheric Radiation, 2nd edn., vol. 84 of International Geophysics Series, Academic Press, San Diego, USA, 2002. 2562

Long, C. N. and Ackerman, T. P.: Identification of clear skies from broadband pyranometer measurements and calculation of downwelling shortwave cloud effects, J. Geophys. Res., 105, 15609–15626, doi:10.1029/2000JD900077, 2000. 2569

Macke, A. and HOPE-Team: The HD(CP)^2 Observational Prototype Experiment HOPE – an overview, Atmos. Chem. Phys., in preparation, 2015. 2559

Macke, A., Mitchell, D. L., and Bremen, L. V.: Monte Carlo radiative transfer calculations for inhomogeneous mixed phase clouds, Phys. Chem. Earth Pt. B, 24, 237–241, doi:10.1016/S1464-1909(98)00044-6, 1999. 2573

Michalsky, J., Dutton, E., Rubes, M., Nelson, D., Stoffel, T., Wesley, M., Splitt, M., and DeLuisi, J.: Optimal measurement of surface shortwave irradiance using current instrumentation, J. Atmos. Ocean. Tech., 16, 55–69, doi:10.1175/1520-0426(1999)016< 0055:OMOSSI> 2.0.CO;2, 1999. 2557

Michalsky, J. J., Harrison, L., and LeBaron, B. A.: Empirical radiometric correction of a silicon photodiode rotating shadowband pyranometer, Sol. Energy, 39, 87–96, 1987. 2575

Michalsky, J. J., Perez, R., Harrison, L., and LeBaron, B. A.: Spectral and temperature correction of silicon photovoltaic solar radiation detectors, Sol. Energy, 47, 299–305, 1991. 2575

Michalsky, J. J., Anderson, G. P., Barnard, J., Delamere, J., Gueymard, C., Kato, S., Kiedron, P., McComiskey, A., and Ricchiazzi, P.: Shortwave radiative closure studies for clear skies during Atmospheric Radiation Measurement 2003 Aerosol Intensive Observation Period, J. Geophys. Res., 111, D14S90, doi:10.1029/2005JD006341, 2006. 2567

Myers, D. R.: Quantitative analysis of spectral impacts on silicon photodiode radiometers, in: SOLAR 2011, NREL/CP-5500-50936, Raleigh, North Carolina, available at: http://www.nrel.gov/docs/fy11osti/50936.pdf, last access: 2 March 2015, 2011. 2574

Ohmura, A., Dutton, E. G., Forgan, B., Fröhlich, C., Gilgen, H., Hegner, H., Heimo, A., König-Langlo, G., McArthur, B., Müller, G., Philipona, R., Pinker, R., Whitlock, C. H., Dehne, K., and Wild, M.: Baseline Surface Radiation Network (BSRN/WCRP): new precision radiometry for climate research, B. Am. Meteorol. Soc., 79, 2115–2136, doi:10.1175/1520-0477(1998)079<2115:BSRNBW>2.0.CO;2, 1998. 2557

Pinker, R. T., Frouin, R., and Li, Z.: A review of satellite methods to derive surface shortwave irradiance, Remote Sens. Environ., 51, 108–124, doi:10.1016/0034-4257(94)00069-Y, 1995. 2557

Robles Gil, S.: The socio-economic benefits of climatological services to the renewable energy sector, WMO Bulletin, Geneva, Switzerland, Tech. Rep., 56, 40–45, 2007. 2557

Roebeling, R. A., van Putten, E., Genovese, G., and Rosema, A.: Application of Meteosat derived meteorological information for crop yield predictions in Europe, Int. J. Remote Sens., 25, 5389–5401, 2004. 2557

Scheirer, R. and Macke, A.: Cloud inhomogeneity and broadband solar fluxes, J. Geophys. Res., 108, 4599, doi:10.1029/2002JD003321, 2003. 2558, 2569

Schmetz, J.: Towards a surface radiation climatology: Retrieval of downward irradiances from satellites, Atmos. Res., 23, 287–321, doi:10.1016/0169-8095(89)90023-9, 1989. 2557

Sengupta, M., Gotseff, P., and Stoffel, T.: Evaluation of Photodiode Thermopile Pyranometers for Photovoltaic Applications, in: 27th European Photovoltaic Solar Energy Conference and Exhibition, Frankfurt, Germany, NREL/CP-5500-56540, available at: http://www.nrel.gov/docs/fy12osti/56540.pdf, last access: 2 March 2015, 2012. 2574

Shi, G. Y., Hayasaka, T., Ohmura, A., Chen, Z. H., Wang, B., Zhao, J. Q., Che, H. Z., and Xu, L.: Data quality assessment and the long-term trend of ground solar radiation in China, J. Appl. Meteorol. Clim., 47, 1006–1016, doi:10.1175/2007JAMC1493.1, 2008. 2571

Stephens, G. L.: Cloud feedbacks in the climate system: a critical review, J. Climate, 18, 237–273, doi:10.1175/JCLI-3243.1, 2005. 2556

van den Hurk, B., Bastiaanssen, W., Pelgrum, H., and van Meijgaard, E.: A new methodology for initialization of soil moisture fields in numerical weather prediction models using METEOSAT and NOAA data, J. Appl. Meteorol., 36, 1271–1283, 1997. 2557

Wild, M., Folini, D., Schär, C., Loeb, N., Dutton, E. G., and König-Langlo, G.: The global energy balance from a surface perspective, Clim. Dynam., 40, 3107–3134, doi:10.1007/s00382-012-1569-8, 2013. 2557

WMO: Measurement of radiation, chapter 7, in: Guide to Meteorological Instruments and Methods of Observations, Tech. Rep. WMO-No. 8, World Meteorological Organization, WMO, Geneva, Switzerland, available at: http://www.wmo.int/pages/prog/gcos/documents/gruanmanuals/CIMO/CIMO_Guide-7th_Edition-2008.pdf, last access: 2 March 2015, 2008. 2557

AMTD

8, 2555–2589, 2015

Table 1. Specifications of an EKO ML-020VM pyranometer sensor (source: http://eko-eu.com/).

Specifications	ML-020VM
Response time (time to reach 95 % response)	10 ms
Zero offset – Thermal radiation (200 $W m^{-2}$)	0 $W m^{-2}$
Zero offset – Temperature change (5 $K h^{-1}$)	0 $W m^{-2}$
Non-stability[a]	± 2 %
Non-linearity[b]	< 0.2 %
Directional response (at 30°/60°/80°)	1/1.5/17 %
Tilt response (at 1000 $W m^{-2}$)	0 %
Temperature response[c]	± 0.5 %
Spectral error (during the day)	± 2–5 %

[a] % change in responsivity per year.
[b] % deviation from responsivity at 1000 $W m^{-2}$ due to change in irradiance.
[c] % deviation due to change in ambient temperature from −10 to +50 °C.

AMTD
8, 2555–2589, 2015

Table 2. Details of observational flags.

Level flag (0–3)	Cleanliness flag (0–10)	Observational flag (1–4)	Remarks
1	1–2	**1**	Good
1 2	3–4 1–4	**2**	Okay, but sometimes spurious
1 2 3	> 4 > 4 1–10	**3**	Bad or ignore completely
0	0	**4**	Missing or no observations

AMTD
8, 2555–2589, 2015

Shortwave surface radiation budget network

B. L. Madhavan et al.

AMTD
8, 2555–2589, 2015

Table 3. Comparison of linear correlation between the time-series measurements of collocated thermopile pyranometers with nearest pyranometers in the network

Day	FZJ vs. PYR76	KIT1 vs. PYR71	KIT2 vs. PYR98
4 May 2013	0.98	0.93	0.95
5 May 2013	0.99	0.78	0.51
30 May 2013	0.99	0.83	0.87

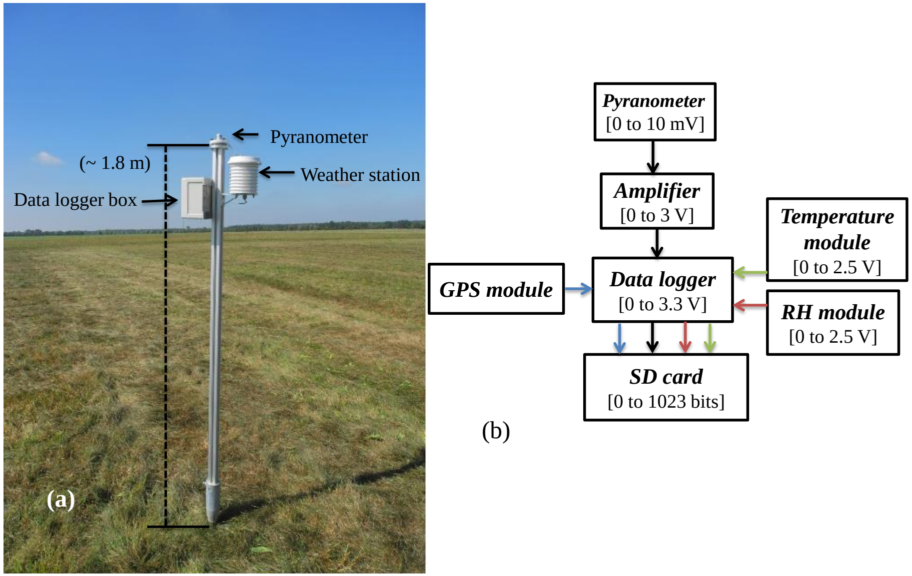

Figure 1. (a) Picture of a pyranometer station in the field, and **(b)** the flow diagram for data recording.

AMTD
8, 2555–2589, 2015

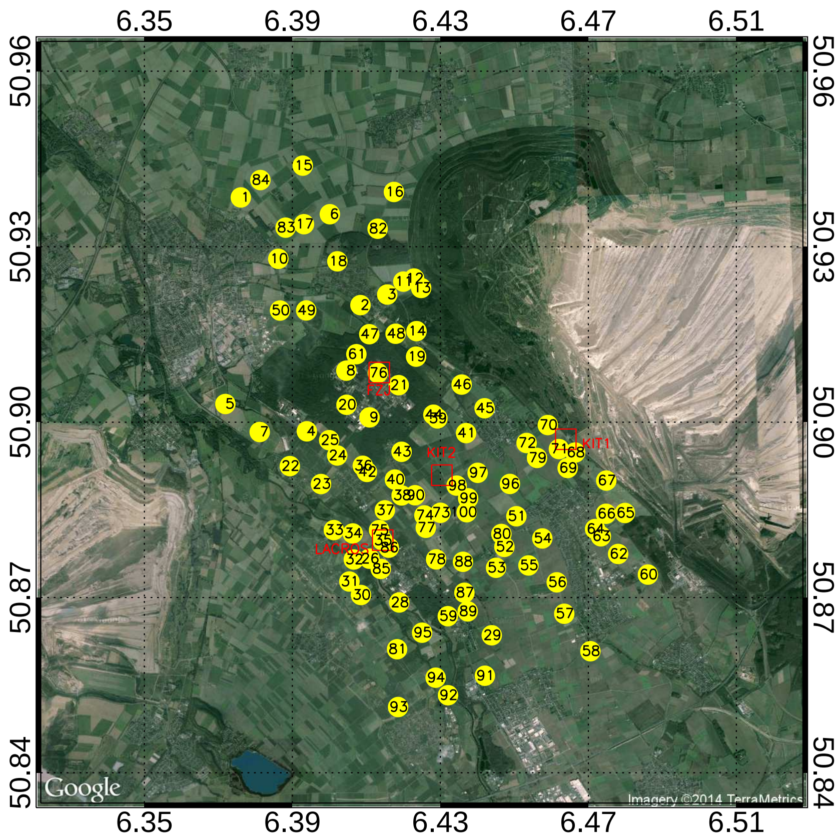

Figure 2. Spatial distribution of pyranometer network during HOPE campaign. Each yellow circle represents a pyranometer station with a unique station identification number. Collocated sites with additional measurements from thermopile pyranometers and a sky imager are marked in open red squares. (Source for background image: Google.)

AMTD
8, 2555–2589, 2015

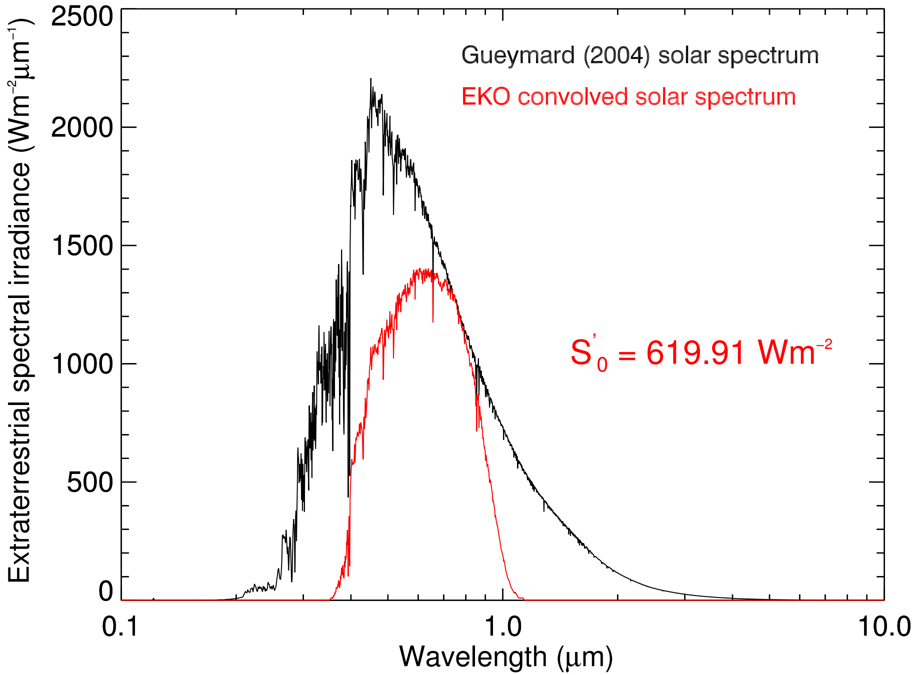

Figure 3. Extraterrestrial solar spectrum of Gueymard (2004) weighted by the spectral response function of the EKO ML-020VM silicon photodiode sensor.

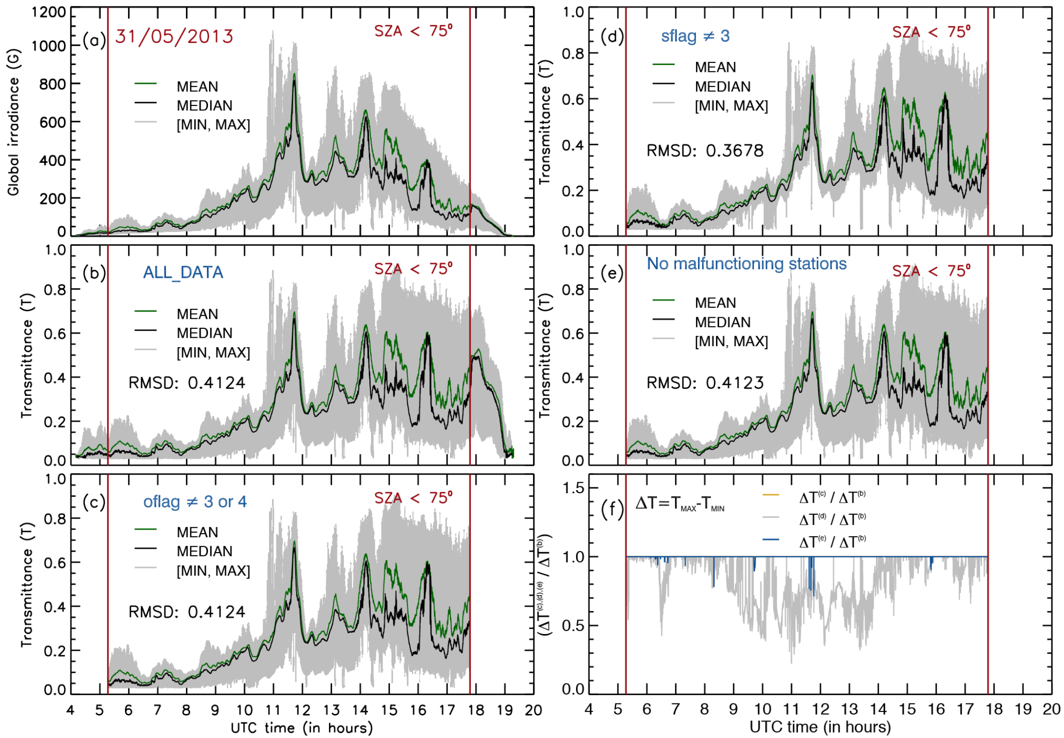

Figure 4. Illustration of our data screening procedure for 31 May 2013. Temporal variability in the mean, median, minimum and maximum values of spatial **(a)** downward global irradiance, and corresponding atmospheric transmittance by **(b)** including all data, **(c)** excluding bad/missing data (oflag ≠ 3 or 4), **(d)** excluding outlier data (sflag ≠ 3), and **(e)** excluding malfunctioning stations. **(f)** Time-series representation of the normalized range of spatial variability in atmospheric transmittance depicted in **(c–e)** with respect to that in **(b)**.

AMTD
8, 2555–2589, 2015

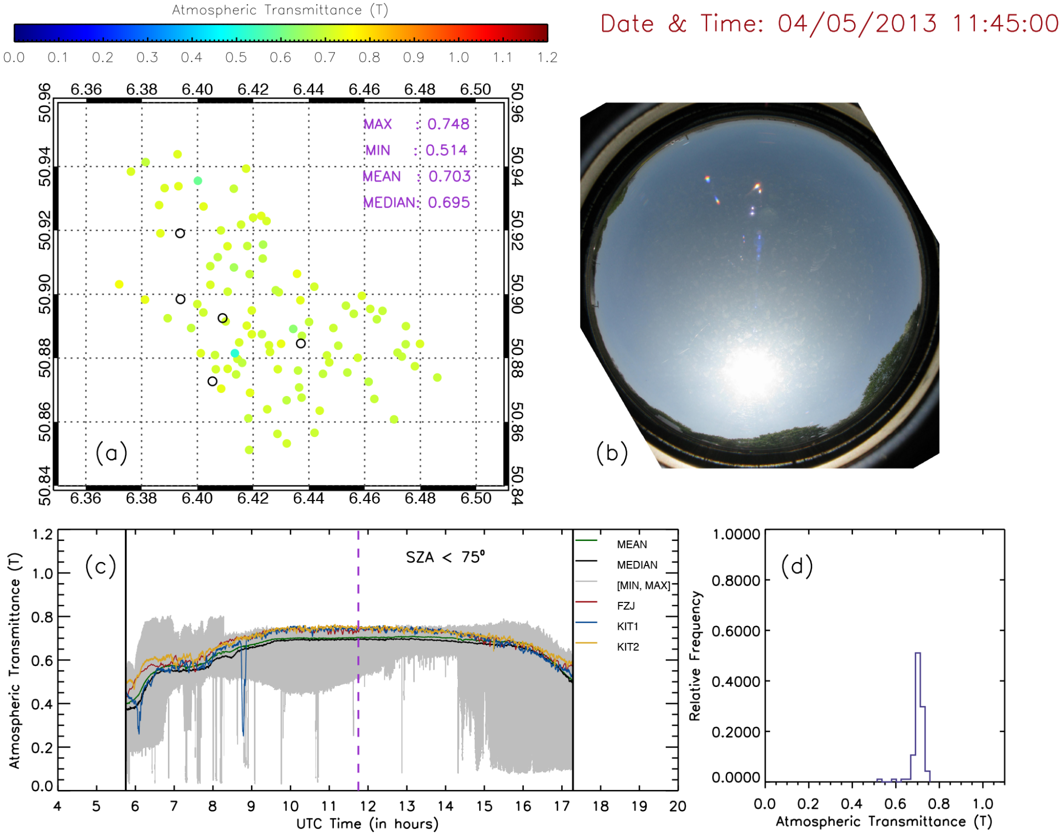

Figure 5. Clear sky – 4 May 2013: **(a)** spatial distribution of derived atmospheric transmittance field with corresponding **(b)** sky imager snapshot at LACROS site for 11:45:00 UTC. **(c)** Temporal variability in the mean, median, minimum and maximum values of the derived spatial atmospheric transmittance values. **(d)** Relative frequency distribution of the spatial transmittance field shown in **(a)**. Missing or malfunctioning stations are represented with open circles in **(a)** and the dashed pink line in **(c)** denotes the time of observation for (**a**, **b** and **d**).

AMTD
8, 2555–2589, 2015

Shortwave surface radiation budget network

B. L. Madhavan et al.

Title Page
Abstract Introduction
Conclusions References
Tables Figures
◀| |▶
◀ ▶
Back Close
Full Screen / Esc
Printer-friendly Version
Interactive Discussion

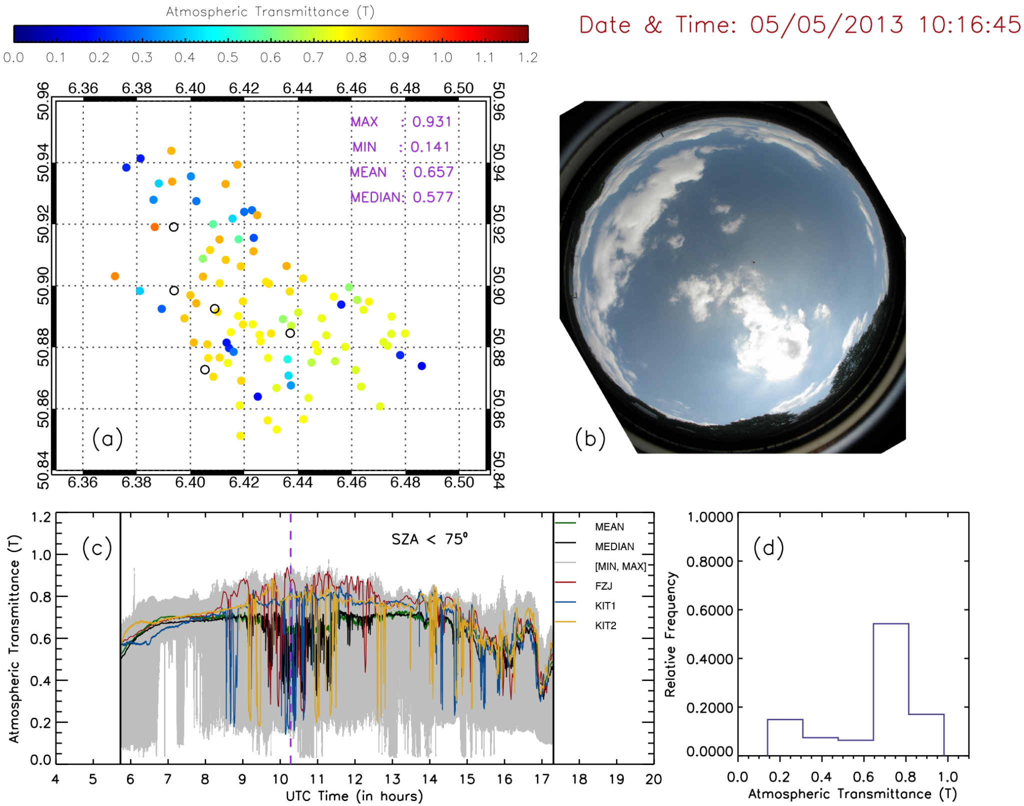

Figure 6. Broken cloudy sky – 5 May 2013: **(a)** spatial distribution of derived atmospheric transmittance field with corresponding **(b)** sky imager snapshot at LACROS site for 10:16:45 UTC. **(c)** Temporal variability in the mean, median, minimum and maximum values of the derived spatial atmospheric transmittance values. **(d)** Relative frequency distribution of the spatial transmittance field shown in **(a)**. Missing or malfunctioning stations are represented with open circles in **(a)** and the dashed pink line in **(c)** denotes the time of observation for (**a**, **b** and **d**).

AMTD
8, 2555–2589, 2015

Shortwave surface radiation budget network

B. L. Madhavan et al.

Title Page
Abstract | Introduction
Conclusions | References
Tables | Figures
◀ | ▶
◀ | ▶
Back | Close
Full Screen / Esc
Printer-friendly Version
Interactive Discussion

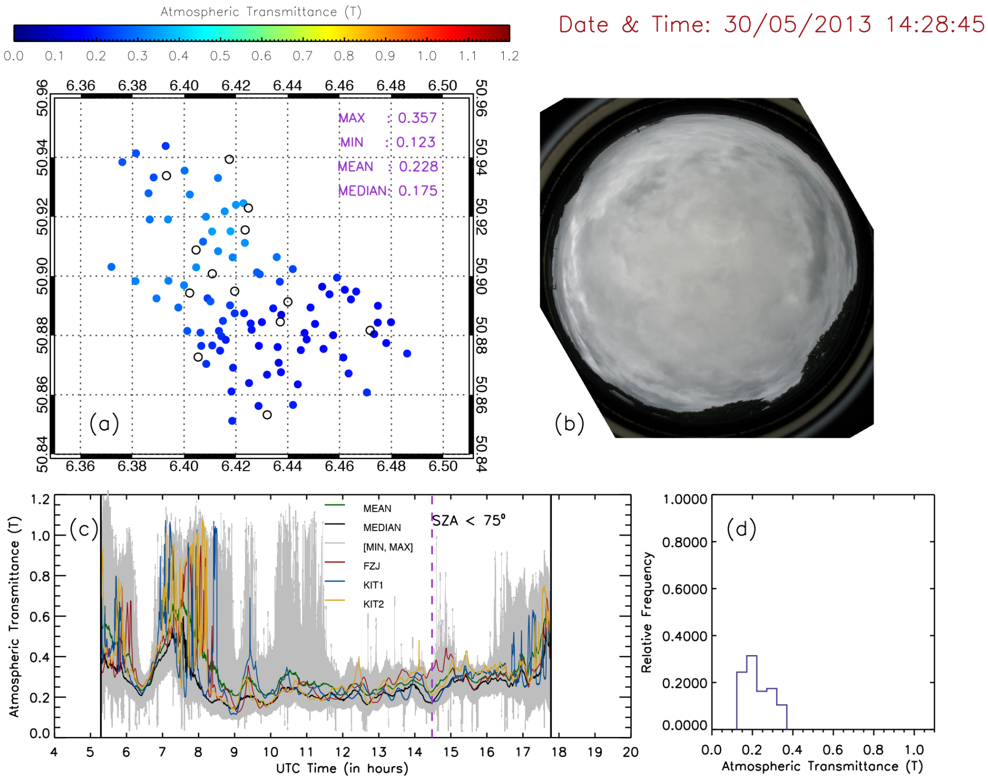

Figure 7. Overcast sky – 30 May 2013: **(a)** spatial distribution of derived atmospheric transmittance field with corresponding **(b)** sky imager snapshot at LACROS site for 14:28:45 UTC. **(c)** Temporal variability in the mean, median, minimum and maximum values of the derived spatial atmospheric transmittance values. **(d)** Relative frequency distribution of the spatial transmittance field shown in **(a)**. Missing or malfunctioning stations are represented with open circles in **(a)** and the dashed pink line in **(c)** denotes the time of observation for (**a**, **b** and **d**).

AMTD
8, 2555–2589, 2015